Time-Resolved Holography with Photoelectrons
Y. Huisman*s*, *et al.*
Science **331**, 61 (2011);
DOI: 10.1126/science.1198450

temperature regime from (*9*), which joins smoothly to the second virial coefficient approximation for S in the high-temperature regime (*20*). The Fig. 3 inset shows the low-temperature behavior, which is about five times the string theory limit (Fig. 3, inset, red dashed line) near the critical energy E_c/E_F = 0.7–0.8 (*9*, *20*). The apparent decrease of the η/s ratio as the energy approaches the ground state $0.48E_F$ (*9*) does not require that the local ratio $\rightarrow 0$ as $T \rightarrow 0$ because contributions from the cloud edges significantly increase S as compared with the local s at the center.

References and Notes

1. K. M. O'Hara, S. L. Hemmer, M. E. Gehm, S. R. Granade, J. E. Thomas, *Science* **298**, 2179 (2002).
2. S. Giorgini, L. P. Pitaevskii, S. Stringari, *Rev. Mod. Phys.* **80**, 1215 (2008).
3. I. Bloch, J. Dalibard, W. Zwerger, *Rev. Mod. Phys.* **80**, 885 (2008).
4. W. Ketterle, M. W. Zwierlein, "Making, probing and understanding ultracold Fermi gases," in *Ultracold Fermi Gases, Proceedings of the International School of Physics "Enrico Fermi,"* Course CLXIV, Varenna, 20 to 30 June 2006 (IOS Press, Amsterdam, 2008).
5. J. Kinast *et al.*, *Science* **307**, 1296 (2005).
6. L. Luo, B. Clancy, J. Joseph, J. Kinast, J. E. Thomas, *Phys. Rev. Lett.* **98**, 080402 (2007).
7. J. T. Stewart, J. P. Gaebler, C. A. Regal, D. S. Jin, *Phys. Rev. Lett.* (2006).
8. H. Hu, P. D. Drummond, X.-J. Liu, *Nat. Phys.* **3**, 469 (2007).
9. L. Luo, J. E. Thomas, *J. Low Temp. Phys.* **154**, 1 (2009).
10. M. Horikoshi, S. Nakajima, M. Ueda, T. Mukaiyama, *Science* **327**, 442 (2010).
11. S. Nascimbène, N. Navon, K. J. Jiang, F. Chevy, C. Salomon, *Nature* **463**, 1057 (2010).
12. P. K. Kovtun, D. T. Son, A. O. Starinets, *Phys. Rev. Lett.* **94**, 111601 (2005).
13. L. P. Csernai, J. I. Kapusta, L. D. McLerran, *Phys. Rev. Lett.* **97**, 152303 (2006).
14. B. A. Gelman, E. V. Shuryak, I. Zahed, *Phys. Rev. A* **72**, 043601 (2005).
15. G. M. Bruun, H. Smith, *Phys. Rev. A* **75**, 043612 (2007).
16. T. Schäfer, *Phys. Rev. A* **76**, 063618 (2007).
17. A. Turlapov *et al.*, *J. Low Temp. Phys.* **150**, 567 (2008).
18. The experiments were performed far from p-wave Feshbach resonances. The relevant threshold energy for p-wave scattering was then comparable with the barrier height. Using the known C_6 coefficients, the barrier height for ^{40}K is 280 μK, whereas for ^{6}Li the barrier height is 8 mK. Hence, for temperatures in the μK range as used in the experiments, p-wave scattering is negligible, and s-wave scattering dominates.
19. J. Kinast, A. Turlapov, J. E. Thomas, *Phys. Rev. Lett.* **94**, 170404 (2005).
20. Materials and methods are available as supporting material on *Science* Online.
21. D. T. Son, *Phys. Rev. Lett.* **98**, 020604 (2007).
22. M. A. Escobedo, M. Mannarelli, C. Manuel, *Phys Rev. A*, http://arxiv.org/abs/0904.3023v2.
23. T.-L. Ho, *Phys. Rev. Lett.* **92**, 090402 (2004).
24. J. E. Thomas, J. Kinast, A. Turlapov, *Phys. Rev. Lett.* **95**, 120402 (2005).
25. T. Schäfer, http://arxiv.org/abs/1008.3876v1.
26. C. Menotti, P. Pedri, S. Stringari, *Phys. Rev. Lett.* **89**, 250402 (2002).
27. P. Massignan, G. M. Bruun, H. Smith, *Phys. Rev. A* **71**, 033607 (2005).
28. We give the damping rate $1/\tau$ for a cylindrically symmetric cigar-shaped trap. For $\delta \equiv (\omega_x - \omega_y)/\sqrt{\omega_x \omega_y} << 1$, with ω_x, ω_y the transverse trap frequencies, $1/\tau$ contains an additional factor $1 - \delta$.
29. H. Guo, D. Wulin, C.-C. Chien, K. Levin, http://arxiv.org/abs/1008.0423v3.
30. E. Taylor, M. Randeria, *Phys. Rev. A* **81**, 053610 (2010).
31. T. Enss, R. Haussmann, W. Zwerger, http://dx.doi.org/10.1016/j.aop.2010.10.002.
32. T. Scäfer, C. Chafin, http://arxiv.org/abs/0912.4236v3.

33. This research is supported by the Physics Divisions of NSF, the Army Research Office, the Air Force Office Office of Sponsored Research, and the Division of Materials Science and Engineering, the Office of Basic Energy Sciences, Office of Science, U.S. Department of Energy. J.E.T. and T.S. thank the ExtreMe Matter Institute (EMMI) for hospitality.

Supporting Online Material

www.sciencemag.org/cgi/content/full/science.1195219/DC1
Materials and Methods
Figs. S1 and S2
References

16 July 2010; accepted 24 November 2010
Published online 9 December 2010;
10.1126/science.1195219

Time-Resolved Holography with Photoelectrons

Y. Huismans,[1]* A. Rouzée,[1,2] A. Gijsbertsen,[1] J. H. Jungmann,[1] A. S. Smolkowska,[1] P. S. W. M. Logman,[1] F. Lépine,[3] C. Cauchy,[3] S. Zamith,[4] T. Marchenko,[5] J. M. Bakker,[6] G. Berden,[6] B. Redlich,[6] A. F. G. van der Meer,[6] H. G. Muller,[1] W. Vermin,[7] K. J. Schafer,[8] M. Spanner,[9] M. Yu. Ivanov,[10] O. Smirnova,[2] D. Bauer,[11] S. V. Popruzhenko,[12] M. J. J. Vrakking[1,2]*

Ionization is the dominant response of atoms and molecules to intense laser fields and is at the basis of several important techniques, such as the generation of attosecond pulses that allow the measurement of electron motion in real time. We present experiments in which metastable xenon atoms were ionized with intense 7-micrometer laser pulses from a free-electron laser. Holographic structures were observed that record underlying electron dynamics on a sublaser-cycle time scale, enabling photoelectron spectroscopy with a time resolution of almost two orders of magnitude higher than the duration of the ionizing pulse.

After a strong laser field ionizes an atom or molecule, the liberated electron is accelerated by the oscillatory laser electric field and driven back toward the ion (*1*). Electron-ion recollision leads to the emission of extreme ultraviolet (XUV) radiation, with a duration that approaches the atomic unit of time (24.2 as) (*2*, *3*) and encodes detailed structural and dynamical information about the atomic or molecular medium used (*4*–*7*). Alternatively, the returning electron may elastically or inelastically scatter (*8*, *9*). These processes benefit from the 10^{11} A/cm^2 electron recollision current incident on the target ion, exceeding current densities used in transmission electron microscopes (*10*). The laser-driven electron motion is fully coherent, allowing one to put into practice the concept of holography (*11*) and to extend it to electron-ion collisions involving laser-ionized and -driven photoelectrons (*9*, *12*, *13*). We show how under suitably chosen experimental conditions, a hologram can be recorded that encodes temporal and spatial information both about the ion (the "target") and the recollision electron (the "source"), opening the way to a new type of ultrafast photoelectron spectroscopy of electron and nuclear dynamics in molecules.

Key to holographic electron imaging is the observation of an interference pattern between a reference wave, which is emitted from the source and does not interact with the target, and a signal wave, which scatters off the target and encodes its structure. The encoded information is stored when the signal wave interferes with the reference wave on a detector. A simple analysis borrowed from ray optics (Fig. 1A) shows that because of path length differences, a phase difference $\Delta\varphi = (k - k_z)z_0$ (where k is the total momentum, k_z is the momentum in the z direction, and z_0 is the distance to the scattering center) arises between the reference and scattered waves, resulting in the pattern shown in Fig. 1B.

To record a clear holographic picture, it is desirable that the reference wave not be influenced by the positively charged target and, therefore, that the electron source is located at some distance from the target, z_0. A suitable way to

[1]FOM Institute AMOLF, Science Park 113, 1098 XG Amsterdam, Netherlands. [2]Max-Born-Institut, Max Born Straße 2A, D-12489 Berlin, Germany. [3]Université Lyon I, CNRS, Laboratoire de Spectrométrie Ionique et Moléculaire, UMR 5579, Bâtiment. Kastler, 43, Boulevard du 11 Novembre 1918, F69622 Villeurbanne Cedex, France. [4]Laboratoire Collisions, Agrégats, Réactivité, Institut de Recherche sur les Systèmes Atomiques et Moléculaires Complexes, UPS, Université de Toulouse and UMR 5589 CNRS, 31062 Toulouse, France. [5]Université Pierre et Marie Curie Université Paris 6, CNRS, UMR 7614, Laboratoire de Chimie Physique-Matière et Rayonnement, 11 rue Pierre et Marie Curie, F-75005 Paris, France. [6]FOM-Institute for Plasma Physics Rijnhuizen, Edisonbaan 14, 3439 MN Nieuwegein, Netherlands. [7]SARA Computing and Networking Services, Science Park 121, 1098 XG Amsterdam, Netherlands. [8]Department of Physics and Astronomy, Louisiana State University (LSU), Baton Rouge, Louisiana 70803–4001, USA. [9]National Research Council of Canada, Ottawa, Ontario K1A 0R6, Canada. [10]Department of Physics, Imperial College, London SW7 2BW, UK. [11]Institut für Physik, Universität Rostock, 18051 Rostock, Germany. [12]Moscow Engineering Physics Institute, National Research Nuclear University, Kashirskoe Shosse 31, Moscow, 115409, Russia.

*To whom correspondence should be addressed. E-mail: huismans@amolf.nl (Y.H.); marc.vrakking@mbi.berlin.de (M.J.J.V.)

accomplish this is tunnel ionization in a strong low-frequency laser field, in which the electron tunnels through a barrier created by the laser field and appears at some distance from the ion.

In the presence of the laser field, the electronic wave function can be written as

$$\psi = \psi_{signal} + \psi_{ref} \quad (1)$$

where ψ_{signal} represents a signal wave packet that oscillates in the laser field and scatters off the target and ψ_{ref} represents a reference wave packet, which only experiences the laser field and does not interact with the target (*14*). To calculate the interference pattern produced by these two terms, we used an extension of the strong field approximation (SFA), which includes the laser field fully and the electron-ion scattering in the first Born approximation (*15*, *16*). The result of the calculation (fig. S3A) (*14*) predicts that in a strong laser field, the holographic fringes remain visible and that the phase difference between the signal and the reference wave packets is

$$\Delta\varphi \approx p_r^2(t_C - t_0^{ref})/2 \quad (2)$$

Here, p_r is the momentum perpendicular to the laser polarization axis, t_C is the time when the signal wave packet scatters off the ion, and t_0^{ref} is the moment of birth of the reference wave packet. Thus, the hologram can be viewed as a pump-probe experiment on the femtosecond-to–sub-femtosecond time scale (fig. S3, B and C), which can encode changes in the scattering potential between t_0^{ref} and t_C, as well as changes in the ionization rate between t_0^{ref} and t_0^{signal}, which is the time of birth of the signal wave packet (*14*). The signal and reference wave packets that produce the holographic pattern originate from the same quarter cycle; thus, subcycle time resolution is encoded, even when long pulses are used.

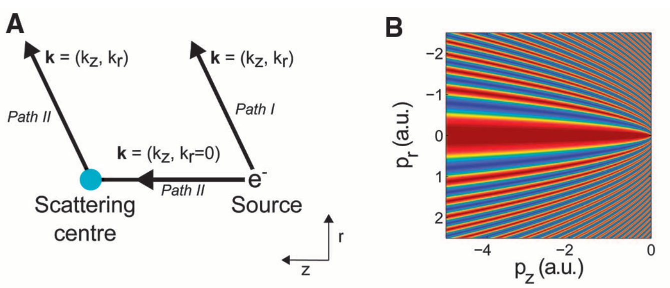

Fig. 1. (**A**) Diagram illustrating the concept of electron holography. Two interfering paths with the same final momentum $\mathbf{k} = (k_z,k_r)$ are indicated. Path I is a reference wave, leaving the source with momentum $\mathbf{k} = (k_z,k_r)$. Path II is a signal wave, incident on the target with $k_r = 0$, $k_z = k = |\mathbf{k}|$ and scattering into $\mathbf{k} = (k_z,k_r)$. The phase difference $\Delta\varphi = (k - k_z)z_0$ that follows from the path length differences leads to interference fringes ~$\cos[(k - k_z)z_0]$. (**B**) Interference pattern generated by a Gaussian wave packet released at a distance $z_0 = 50$ atomic units (a.u.) from a scattering center, with no laser field present. A hologram is created as a result of interference between a scattering-signal wave packet and a direct-reference wave packet.

A crucial aspect in our holographic imaging approach is the existence of a large electron oscillation amplitude of $\alpha >> 1$ Å and a large average oscillation energy $U_p >> \hbar\omega_{laser}$, where ω_{laser} is the laser frequency and $\hbar$ is Planck's constant h divided by 2π. In experiments with 800 nm radiation, these requirements lead to high laser intensities ($I \sim 10^{14}$ W/cm^2) that can only be applied to ground-state atoms and molecules with a large ionization potential. To make recollision-based imaging possible at lower intensities, the laser wavelength λ_{laser} must be increased because both α and U_p scale as λ_{laser}^2.

To demonstrate the strong-field electron holography experimentally, metastable (6 s) xenon atoms were ionized with 7-µm mid-infrared (mid-IR) radiation from the FELICE (Free Electron Laser for Intra-Cavity Experiments) beamline at the Free Electron Laser for Infrared Experiments (FELIX) facility (fig. S1) (*14*, *17*). The use of a large λ_{laser} in combination with a modest ionization potential (IP = 3.8 eV) allowed the preparation of electron wave packets born at large $z_0 = IP/F_{laser}$, where F_{laser} is the laser field strength, displaying a large excursion α_0, without the need for a very high laser intensity (7×10^{11} W/cm^2), and remaining in the tunneling regime $\left[\gamma = \left(\frac{\omega_{laser}}{F_{laser}}\right)\sqrt{2IP} < 1\right]$. Angle-resolved photoelectron spectra were recorded with a velocity map imaging spectrometer (VMI) (*18*) integrated into the FELICE laser cavity. The metastable xenon atoms were exposed to a train of 5000 mid-IR laser pulses separated by 1 ns.

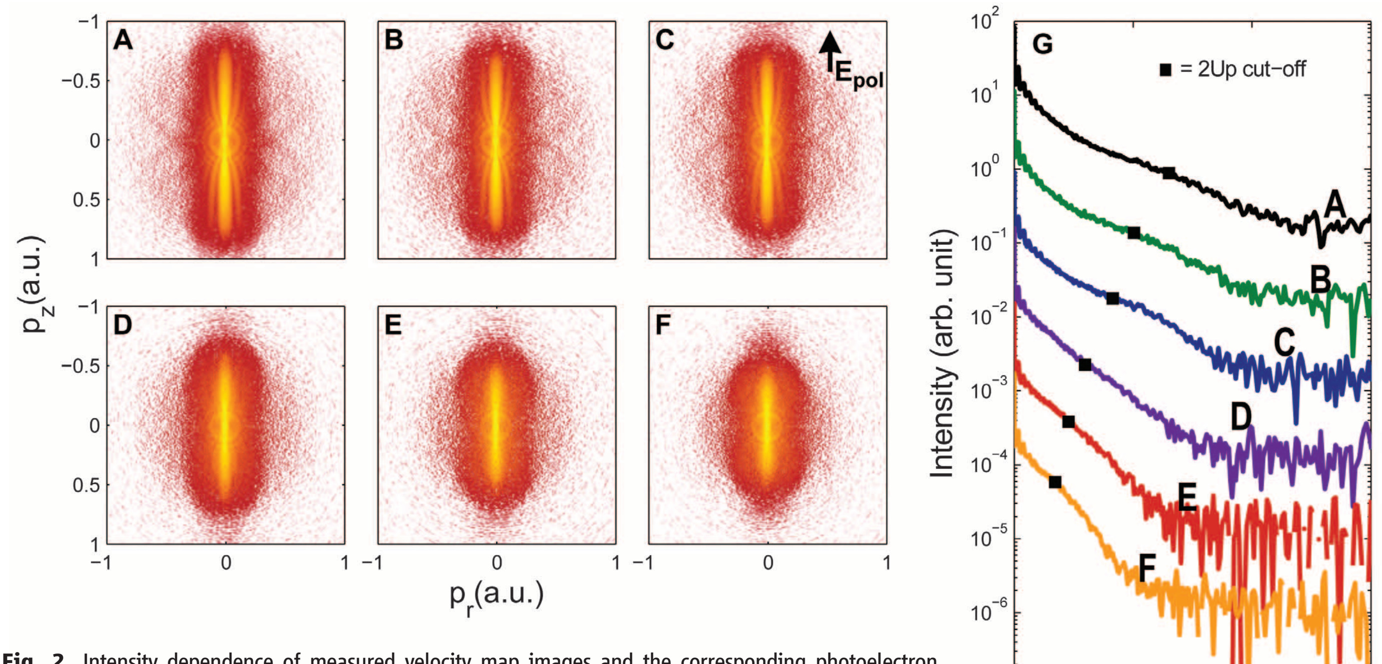

Fig. 2. Intensity dependence of measured velocity map images and the corresponding photoelectron kinetic energy distributions. (**A**) 7.1×10^{11} W/cm^2; (**B**) 5.5×10^{11} W/cm^2; (**C**) 4.5×10^{11} W/cm^2; (**D**) 3.2×10^{11} W/cm^2; (**E**) 2.5×10^{11} W/cm^2; and (**F**) 1.9×10^{11} W/cm^2. (**G**) Angle-integrated photoelectron spectra. Squares indicate the energy that corresponds to the classical $2U_p$ cutoff energy.

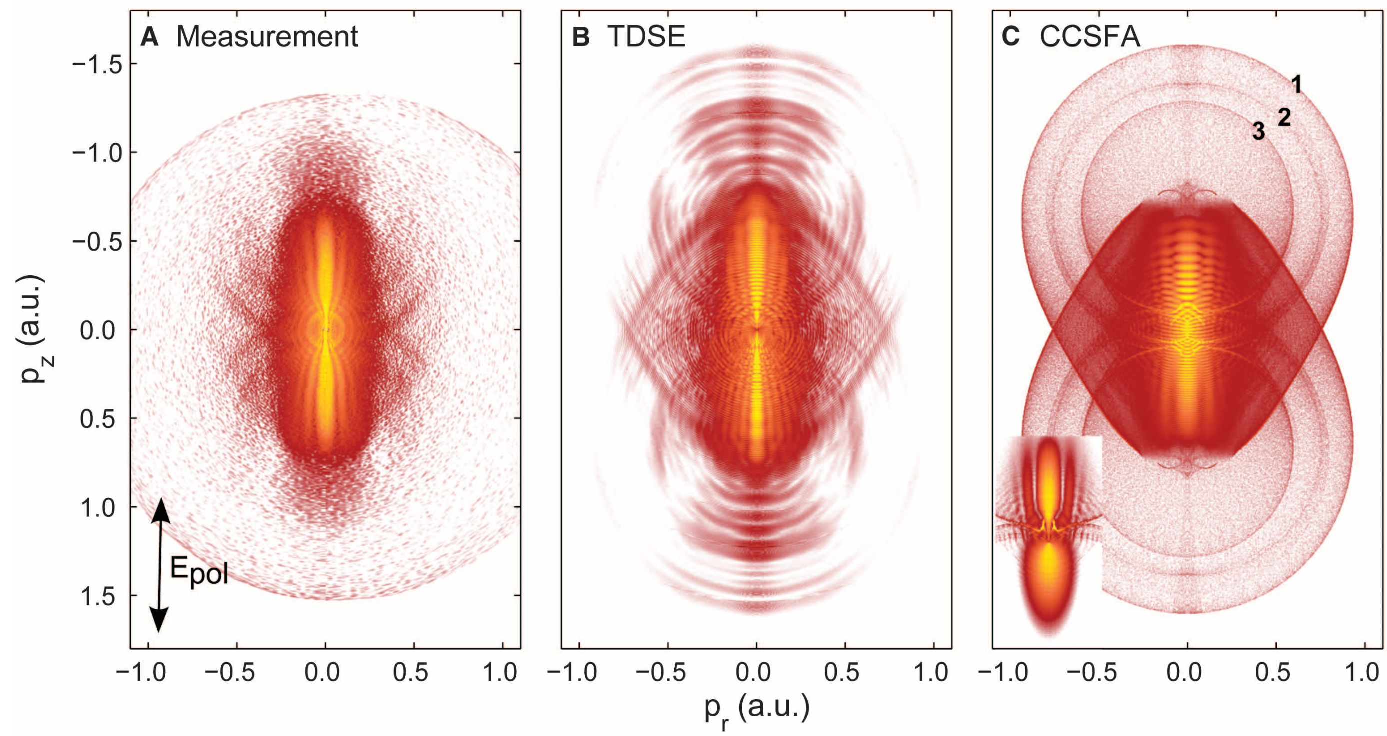

Fig. 3. Comparison of an experimental two-dimensional photo-electron velocity map image with calculations (CCSFA and TDSE). (**A**) Four-hour-long measurement of the ionization of metastable xenon under conditions similar to those used in the measurements shown in Fig. 2A. (**B**) TDSE calculation for ionization of argon (5 s) (IP = 0.14 a.u., four-cycle flat-top 7-μm pulse, peak field strength of 0.0045 a.u.). (**C**) CCSFA calculation for ionization of a model hydrogenic atom (IP = 0.14 a.u., λ_{laser} = 7 μm, peak field strength of 0.0045 a.u.). (Inset) CCSFA single half-cycle calculation, illustrating that the side-lobes are due to an interference between two trajectories that leave the atom within the same half-cycle.

Varying the position of the experimental apparatus along the laser propagation axis allowed the peak intensity to be tuned by approximately a factor of five. Figure 2, A to F, shows a dominant electron emission along the laser polarization axis, with a high-energy cutoff (Fig. 2G) that agrees well with the classical expectation $E_{cutoff} = F_{laser}^2/2\omega_{laser}^2$. In Fig. 3A, "side-lobes" are observed that extend from low to high momentum and run parallel to the laser polarization axis for high momenta. These side-lobes qualitatively agree with the patterns calculated in fig. S3A and result from a holographic interference. Additionally, a number of weaker transverse structures extend sideways approximately orthogonal to the laser polarization. Neither of these structures should be confused with the so-called side-lobes, "wings," or "rings" caused by backscattered electrons that were observed in higher-order above-threshold ionization (*19*, *20*), nor are they related to the interferences observed in recent experiments on ionization of helium by a few-cycle pulse (*21*).

The experimental observation of holographic interferences is confirmed through full time-dependent Schrödinger equation (TDSE) calculations, which show the same fringe pattern (Fig. 3B) (*22*). The fringe spacing agrees with the experiment and is reduced compared with the SFA-based calculation (fig. S3A), in which the long-range Coulomb potential was neglected.

Insight into the role of the Coulomb potential was gained by performing semiclassical calculations with the Coulomb-corrected strong-field approximation (CCSFA) (*14*) (*23*). In these calculations, complex quantum trajectories are calculated that, after tunneling, include the Coulomb interaction of the electron in the classically allowed region. The spectrum is calculated by summing contributions from different trajectories, including their phases (*14*). The results (Fig.

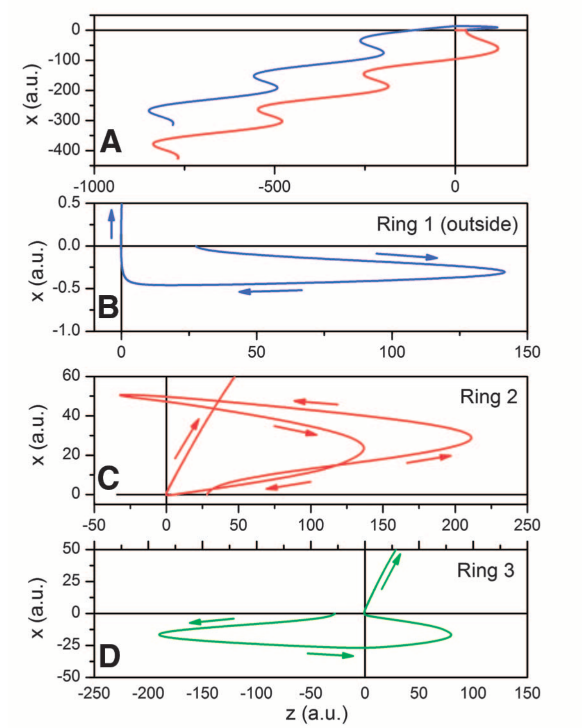

Fig. 4. (**A**) Two trajectories that lead to the formation of electrons with a final momentum of p_r = −0.01 a.u. and p_z = −0.46 a.u. The red trajectory corresponds to an electron that only weakly interacts with the ionic core. The blue trajectory corresponds to an electron that strongly interacts with the ionic core and that undergoes Coulomb focusing. (**B** to **D**) Recollision trajectories, illustrating the occurrence of a recollision at the first (ring 1), second (ring 3), or third (ring 2) opportunity. The highest kinetic energy of electrons on ring 1 is 1.289 a.u. (10.75 U_p).

3C) quantitatively reproduce the main features discussed above. Inspection of the trajectories responsible for the side-lobes shows that these trajectories can indeed be considered as a reference and scattered wave packet, creating a hologram (Fig. 4A).

The efficiency of electron-ion recollision drops dramatically with increasing λ_{laser} because of spreading of the wave packet between ionization and recollision. Still, a clear hologram can be observed at 7 μm. Two effects make this possible. First, the hologram results from a heterodyne experiment, in which a weaker signal is mixed with a stronger signal. Second, to create a clear reference a large-impact parameter is needed in order to limit the interaction with the Coulomb field. For large λ_{laser}, a small p_r already leads to large-impact parameters because of the long excursion time between ionization and recollision.

Inspection of the electron trajectories contributing to the transverse structures (Fig. 3) reveals that they are due to recollision events in which the scattering does not occur on the first opportunity but on the second or third (*20*, *24*, *25*). Typical examples of these trajectories are shown in Fig. 4, B to D. One, respectively two glancing electron-ion collisions can be observed before the real recollision takes place. Usually, these rare events do not leave an imprint on the photoelectron spectrum. However, the combination of a long laser wavelength and Coulomb focusing (*24*) increases the probability because a small deviation introduced by the Coulomb potential can be sufficient to focus the returning wave packet onto the ion.

In our model study on the ionization of metastable xenon, we have experimentally shown the possibility to record holographic structures. Furthermore, our theoretical exploration shows that the hologram stores spatial and temporal information about the core- and electron dynamics. This offers opportunities to extend strong-field holography to more complicated systems and to use it to time-resolve electron-dynamics. As revealed in recent experiments (*6*, *26*), electron-ion recollision phenomena encode hole dynamics that occur in ions during the first few femtoseconds after strong-field ionization. When properly implemented with the use of a long-wavelength-driving laser, photo-electron holography appears especially well suited for studying this type of dynamics, in particular in molecules with a low binding energy that cannot easily be studied by other means.

References and Notes

1. P. B. Corkum, *Phys. Rev. Lett.* **71**, 1994 (1993).
2. F. Krausz, M. Y. Ivanov, *Rev. Mod. Phys.* **81**, 163 (2009).
3. M. F. Kling, M. J. J. Vrakking, *Annu. Rev. Phys. Chem.* **59**, 463 (2008).
4. J. Itatani *et al.*, *Nature* **432**, 867 (2004).
5. D. Shafir, Y. Mairesse, D. M. Villeneuve, P. B. Corkum, N. Dudovich, *Nat. Phys.* **5**, 412 (2009).
6. O. Smirnova *et al.*, *Nature* **460**, 972 (2009).
7. S. Baker *et al.*, *Science* **312**, 424 (2006).
8. M. Meckel *et al.*, *Science* **320**, 1478 (2008).
9. M. Spanner, O. Smirnova, P. B. Corkum, M. Y. Ivanov, *J. Phys. At. Mol. Opt. Phys.* **37**, L243 (2004).
10. H. Niikura *et al.*, *Nature* **417**, 917 (2002).
11. D. Gabor, *Nobel Lectures, Physics 1971-1980* (World Scientific, Singapore, 1992).
12. G. G. Paulus *et al.*, *Phys. Rev. Lett.* **84**, 3791 (2000).
13. J. Mauritsson *et al.*, *Phys. Rev. Lett.* **100**, 073003 (2008).
14. Materials and methods are available as supporting material on *Science* Online.
15. W. Becker, A. Lohr, M. Kleber, *J. Phys. At. Mol. Opt. Phys.* **27**, L325 (1994).
16. M. Lewenstein, K. C. Kulander, K. J. Schafer, P. H. Bucksbaum, *Phys. Rev. A* **51**, 1495 (1995).
17. J. M. Bakker *et al.*, *J. Chem. Phys.* **132**, 074305 (2010).
18. A. T. J. B. Eppink, D. H. Parker, *Rev. Sci. Instrum.* **68**, 3477 (1997).
19. B. R. Yang *et al.*, *Phys. Rev. Lett.* **71**, 3770 (1993).
20. G. G. Paulus, W. Becker, W. Nicklich, H. Walther, *J. Phys. At. Mol. Opt. Phys.* **27**, L703 (1994).
21. R. Gopal *et al.*, *Phys. Rev. Lett.* **103**, 053001 (2009).
22. H. G. Muller, *Laser Phys.* **9**, 138 (1999).
23. S. V. Popruzhenko, D. Bauer, *J. Mod. Opt.* **55**, 2573 (2008).
24. T. Brabec, M. Y. Ivanov, P. B. Corkum, *Phys. Rev. A* **54**, R2551 (1996).
25. G. L. Yudin, M. Y. Ivanov, *Phys. Rev. A* **63**, 033404 (2001).
26. Y. Mairesse *et al.*, *Phys. Rev. Lett.* **104**, 213601 (2010).

27. We acknowledge R. Kemper, H. Schoenmaker, A. de Snaijer, I. Cerjak, and the staff at the FELIX facility for their great technical assistance. This work is part of the research program of FOM, which is financially supported by the Nederlandse organisatie voor Wetenschappelijk Onderzoek (NWO). K.J.S. is supported by NSF grant PHY-0701372 and the Ball Professorship at LSU. M.Y.I. is supported by Science and Innovation grant EP/E036112/1 of the Engineering and Physical Sciences Research Council. O.S. acknowledges a Leibniz SAW award.

Supporting Online Material

www.sciencemag.org/cgi/content/full/science.1198450/DC1
Materials and Methods
SOM Text
Figs. S1 to S5
References

29 September 2010; accepted 7 December 2010
Published online 6 December 2010;
10.1126/science.1198450

Spin Crossover in Ferropericlase at High Pressure: A Seismologically Transparent Transition?

Daniele Antonangeli,[1,2]* Julien Siebert,[1,2] Chantel M. Aracne,[2] Daniel L. Farber,[2,3] A. Bosak,[4] M. Hoesch,[4] M. Krisch,[4] Frederick J. Ryerson,[2] Guillaume Fiquet,[1] James Badro[1,2]

Seismic discontinuities in Earth typically arise from structural, chemical, or temperature variations with increasing depth. The pressure-induced iron spin state transition in the lower mantle may influence seismic wave velocities by changing the elasticity of iron-bearing minerals, but no seismological evidence of an anomaly exists. Inelastic x-ray scattering measurements on $(Mg_{0.83}Fe_{0.17})O$-ferropericlase at pressures across the spin transition show effects limited to the only shear moduli of the elastic tensor. This explains the absence of deviation in the aggregate seismic velocities and, thus, the lack of a one-dimensional seismic signature of the spin crossover. The spin state transition does, however, influence shear anisotropy of ferropericlase and should contribute to the seismic shear wave anisotropy of the lower mantle.

The characterization of pressure- and temperature-induced transformations in mantle minerals and their connection to seismic discontinuities aid in the understanding of Earth's interior. In this sense, the series of phase transformations that occurs in olivine—which with increasing pressure first transforms to wadsleyite, then to ringwoodite, and then breaks down into ferropericlase and perovskite—is emblematic. These phase changes are accompanied by density and sound-velocity variations that are responsible for the main seismic discontinuities in the upper mantle (*1*).

In contrast, the recently discovered iron spin-state transition—where compression favors the electron spin pairing, with the system changing from a high-spin to a low-spin state—in both ferropericlase (*2*) and perovskite (*3*), the two main phases of the lower mantle, does not clearly relate to any seismic signature, although effects on mantle density and seismic wave velocity have been anticipated (*4*–*8*). In ferropericlase, the spin transition occurs without structural changes (*4*, *9*), but experimental (*10*) and theoretical (*11*) studies suggest large softening of all the elastic moduli and, consequently, a major decrease in the aggregate sound velocities. Thus, at pressure and temperature conditions of the lower mantle, such an effect should be associated to a broad seismic anomaly (*12*) that, conversely, is not observed (*13*, *14*).

Here we present inelastic x-ray scattering (IXS) measurements on $(Mg_{0.83}Fe_{0.17})O$-ferropericlase across the spin transition and up to 70 GPa (*15*). We obtained the complete elastic tensor (that is,

[1]Institut de Minéralogie et de Physique des Milieux Condensés, UMR CNRS 7590, Institut de Physique du Globe de Paris, Université Pierre et Marie Curie, Université Paris Diderot, 75005 Paris, France. [2]Lawrence Livermore National Laboratory, Livermore, CA 94550, USA. [3]Department of Earth and Planetary Sciences, University of California, Santa Cruz, Santa Cruz, CA, 95064, USA. [4]European Synchrotron Radiation Facility, BP 220, 38043 Grenoble Cedex, France.

*To whom correspondence should be addressed. E-mail: daniele.antonangeli@impmc.upmc.fr